Supplementary Information

Unraveling the role of crystallization kinetics for fibrillar morphology optimization in all-polymer solar cells

Zhiyuan Yang,[a] Lei Yu[a], Qiaoyu Guo,[b] Fei Xie,[b] Xuechen Jiao,[b] Lei Ying,[a] Wenkai Zhong*[a], Fei Huang*[a]

[a] Institute of Polymer Optoelectronic Materials and Devices, Guangdong Basic Research Center of Excellence for Energy & Information Polymer Materials, State Key Laboratory of Luminescent Materials and Devices, South China University of Technology, Guangzhou 510640, China
E-mail: wkzhong@scut.edu.cn; msfhuang@scut.edu.cn

[b] National Synchrotron Radiation Laboratory, University of Science and Technology of China, Hefei, China

Experimental Section

Materials and synthesis

Both PBTA-BO and N2200 were purchased from obtained from Dongguan VoltAmp Optoelectronics Technology Company. Solvent and additives were purchased from Sigma or TCI Chemical Co. and used as received.

Device fabrication and characterization

The conventional structure of ITO/PEDOT:PSS/active layer/PNDIT-F3N-Br/Ag was used to fabricate all-PSC devices. The indium tin oxide (ITO) substrates were cleaned sequentially by sonication with detergent, deionized water, and isopropanol. After being dried in an oven, the substrates were treated with an oxygen plasma for 4 mins and then coated with PEDOT:PSS (CLEVIOS P VP Al 4083) as anode interface at 4000 rpm for 30 s. After annealing at 150 °C on a hot plate for 15 min, the substrates were transferred into a nitrogen-filled glovebox. The PBTA-BO and N2200 were dissolved in MeTHF with weight ratio of 2:1 at a concentration of 4 mg mL^{-1} for PBTA-BO. The solution was stirred on a hotplate at 120 °C for 30 min to ensure complete dissolution. Subsequently, DIO or DPE were added as solvent additives, followed by additional stirring at 120 °C for 10 min. The dissolved active layer solution was spin-coated onto the PEDOT:PSS layer at 1600-2000 rpm, yielding film thicnkness of ~120 nm, followed by thermal annealing at 120 °C for 10 min on a hotplate. Then, the cathode interface PDINT-F3N-Br (1 mg mL^{-1} in methanol) was spin-coated at 3000 rpm atop the active layer. Finally, 100 nm Ag was thermally deposited on top of the interface through a shadow mask in a vacuum chamber at a pressure of around 1×10^{-6} mbar. The effective area of the device was defined to 0.0516 cm^2, and further confined to 0.04 cm^2 by a metal aperture for J-V curve tests. The J-V curves were measured with Keithley 2400 source meter under 1 sun, AM 1.5G solar simulator (Enlitech SS-F5). The light intensity was calibrated by a standard silicon solar cell before the test. The EQE spectra were recorded with a QE-R measurement system (Enlitech QE-R3011).

For energy loss (E_{loss}) measurements of solar cell devices, electroluminescence quantum efficiency ($\mathrm{EQE_{EL}}$) was tested under dark conditions when charge carriers are injected into the device (REPS PECT-600, Enlitech). The energy loss ($E_{\mathrm{loss}} = E_{\mathrm{g}} - qV_{\mathrm{OC}}$) can be decomposed into three components. ΔE_1 arises from the fundamental mismatch between the directional sunlight (received within a narrow solid angle) and the omnidirectional radiative recombination from photons emitted above the bandgap. This loss is intrinsic to all solar cells and typically amounts to 0.25 eV or more. ΔE_2 represents additional radiative losses due to sub-bandgap absorption. ΔE_3 corresponds to non-radiative recombination losses and can be calculated using $\Delta \mathrm{E}_3 = -kT\ln(\mathrm{EQE_{EL}})$.

The device physics, including photo-CELIV, *C-V*, *C-F* characteritisc were probed by a PAIOS system (Fluxim). For *C-V* characteristics, the devices were measured in the dark across a bias range of -3 V to 2 V. The interfacial carrier distribution was analyzed using the Mott-Schottky relation:

$$\frac{1}{C^2} = \frac{2(V_{Bi} - V)}{A^2 q \varepsilon_0 \varepsilon_r N_A}$$

where C denotes capacitance, V_{bi} the built-in potential, A the active area, ε_r the relative permittivity, and N the charge density.

For *C-F* characteristics, the devices were measured under dark conditions across a frequency range of 10 MHz to 1 Hz to probe charge trapping phenomena and dielectric properties. The tDoS energy distribution was evaluated through analysis of the angular frequency-dependent capacitance response, as described by the relation:

$$N_T\left(E_\omega\right) = -\frac{V_{bi}}{qW} \cdot \frac{dC}{d\omega} \cdot \frac{\omega}{kT}$$

where ω is the angular frequency, C is the capacitance, q is the elementary charge, k is the Boltzmann's constant, T is absolute temperature. V_{bi} and W are the built-in potential and depletion width, respectively, which were extracted from the Mott-Schottky analysis. The applied angular frequency ω defines an energetic demarcation.

$$E_\omega = kT\ln\left(\frac{\omega_0}{\omega}\right)$$

where ω_0 is the attempt-to-escape frequency. The trap states below the energy demarcation can capture or emit charges with the given ω and contribute to the capacitance.

General characterizations

UV-vis absorption spectra of thin-films were measured using a Shimadzu UV-3600 UV-vis-NIR spectrophotometer. The solubility of the polymers in the solvent (MTHF, DPE, or DIO) was determined at room temperature (~25 °C) by preparing a saturated solution. This involved incrementally adding an excess amount of the polymer to a known volume of solvent and stirring vigorously for three hours to reach equilibrium. After stirring ceased, the suspension was allowed to stand undisturbed to ensure complete precipitation of undissolved polymer and phase separation. The clear supernatant liquid was then carefully withdrawn and analyzed using UV-vis-NIR spectroscopy. The absorbance (A) of this saturated solution was compared with that of a reference solution of know concentrations of the same polymer in the same solvent. Then the saturated concentration, representing the maximum solubiltiy, was calculated using the Beer-Lambert law: $A = \varepsilon \times l \times c$, where ε is the molar attenuaton cofficient, l is the optical path length, and c is the concentration.

GIWAXS was conducted at beamline 7.3.3 of the Advanced Light Source (ALS). The incident X-ray energy was 10 keV. The incident angle of X-ray beam to the sample surface was fixed at 0.16°. The sample-to-detector distance (SDD) was calibrated to 280 mm using silver behenate standard. The scattering signals were collected by a Pilatus 2M detector (pixel size: 0.172 mm×0.172 mm) under continuous helium purging. *In situ* GIWAXS was conducted during slot-die coating with continuous 0.2 s exposure time per frame, enabling real-time tracking of molecular ordering from solution to solid film. *In situ* GISAXS was performed at the same beamline with the same experimental setup and data collection, but the SDD was set to 3700 mm. RSoXS was performed at Jinhua Beamline at the National Synchrotron Research Laboratory. All blend films were prepared on PEDOT:PSS/Si wafer, with the conditions same to device fabrication. The samples were then floated on water, leading to disolution of PEDOT:PSS and leaving the blend films on water. The blend films were then transferred on silicon nitride windows for RSoXS measurement in transmission mode. Each scattering image was captured using a Greateyes Lotti 4k4k CCD camera with a pixel size of 0.015 mm × 0.015 mm. AFM-IR was performed by Anasys nanoIR3 (Bruker). Stress-strain (σ-ε) measurements were performed using a tensile stage (HY-0230, Shanghai Hengyi Precision Instrument Co., Ltd). The thin films were spin-coated on PEDOT:PSS-coated substrates, released by dissolving the PEDOT:PSS layer in water, and then mounted onto frosted aluminum clamps. Uniaxial tensile testing was conducted at a constant strain rate of 0.01 mm min^{-1}. Engineering stress (σ) and strain (ε) were calculated as: $Stress = F / (A \times B)$ and $\text{S}train = \Delta l / l_0$, where F is the applied force (measured by a high-sensitivity load cell), A is the film width, B is the film thickness, Δl is the elongation, and l_0 is the initial distance between the clamps.

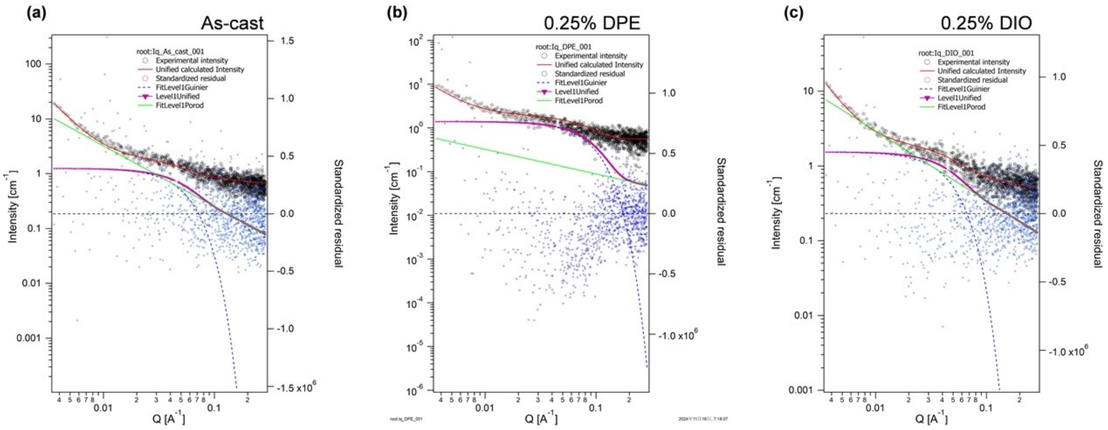

Fig. S1 Unified fit of *I-q* curves for the first frame of in situ GISAXS of PBTA-BO:N2200 blends: (a) as-cast, (b) with 0.25% DPE, and (c) with 0.25% DIO.

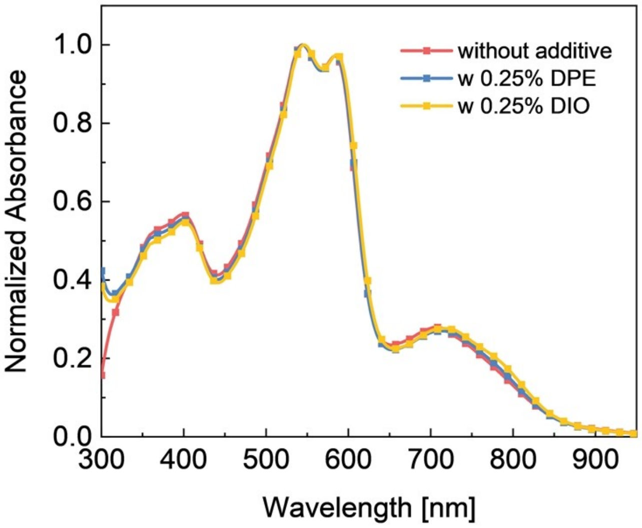

Fig. S2 Normalized UV-vis absorption spectra of additive-free, 0.25% DPE-containing, and 0.25% DIO-containing PBTA-BO:N2200 blend solutions.

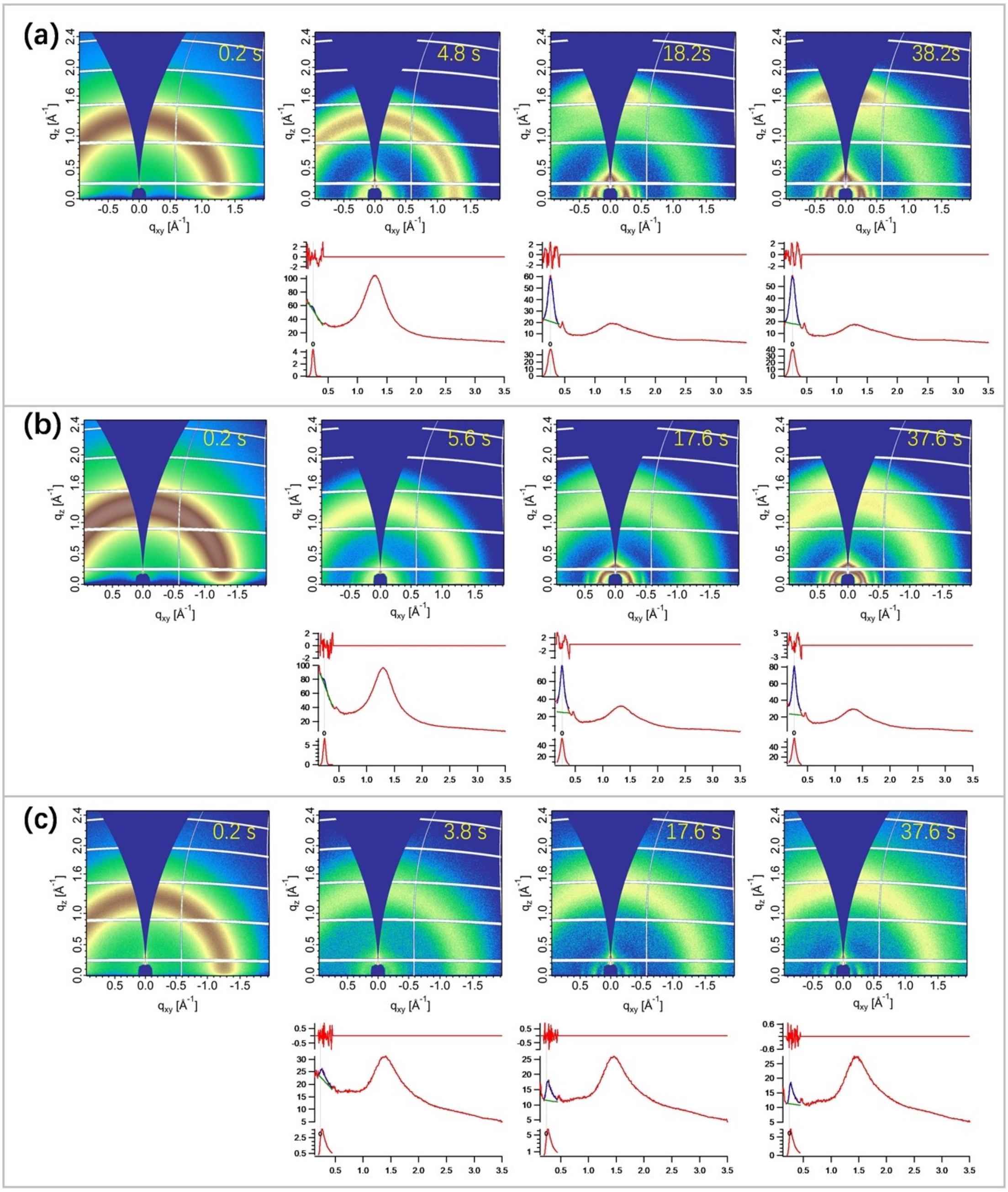

Fig. S3 Representative 2D GIWAXS patterns at different time frames along with fits of the (100) peak from the *I-q* curves in the IP direction, representing different stages: the initial solution state before drying begins (0.2 s), the early stage when the (100) peak appeared (3.8-5.6 s), an intermediate stage (17.6-18.2 s), and the final state where the *in situ* experiments were terminated (37.6-38.2 s).

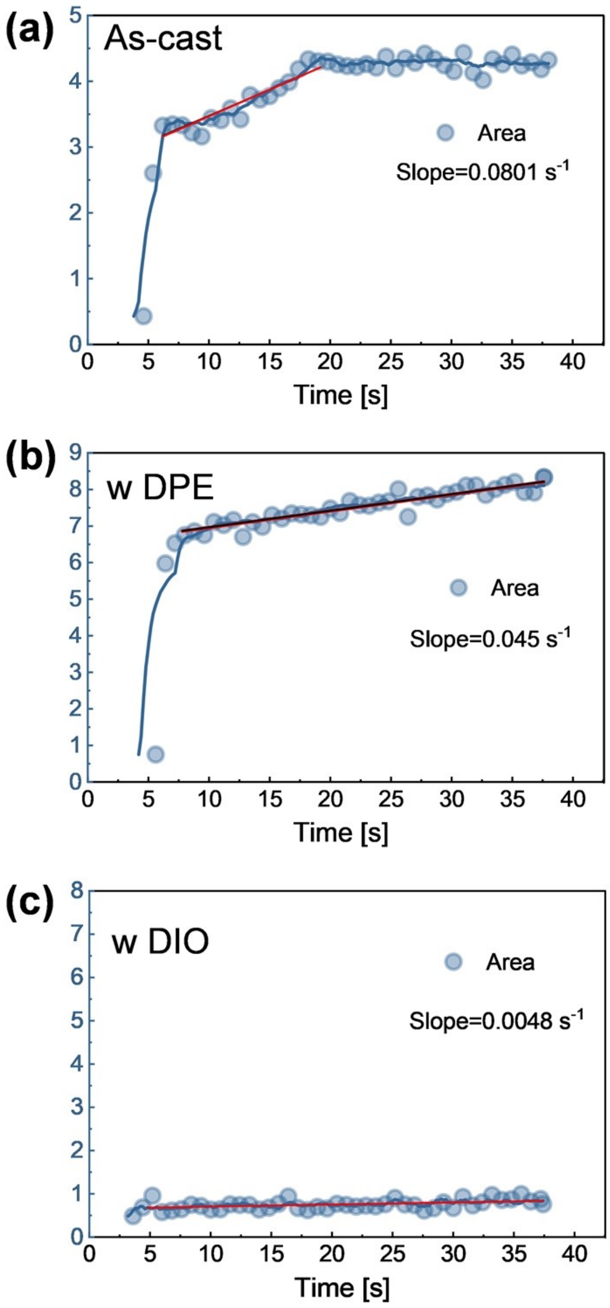

Fig. S4 Linear fitting of the peak area as a function of drying time in the slow crystallization region: (a) as-cast blend, (b) 0.25% DPE-processed blend, and (c) 0.25% DIO-processed blend. Slopes of the fitted lines (red) represent crystallization rates.

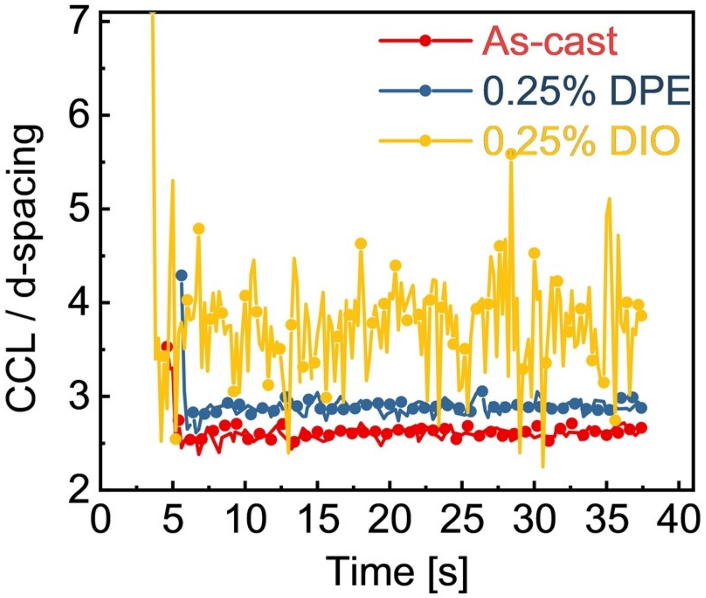

Fig. S5 The calculated CCL/*d*-spacing of lamellar reflections at each time frame for *in situ* GIWAXS.

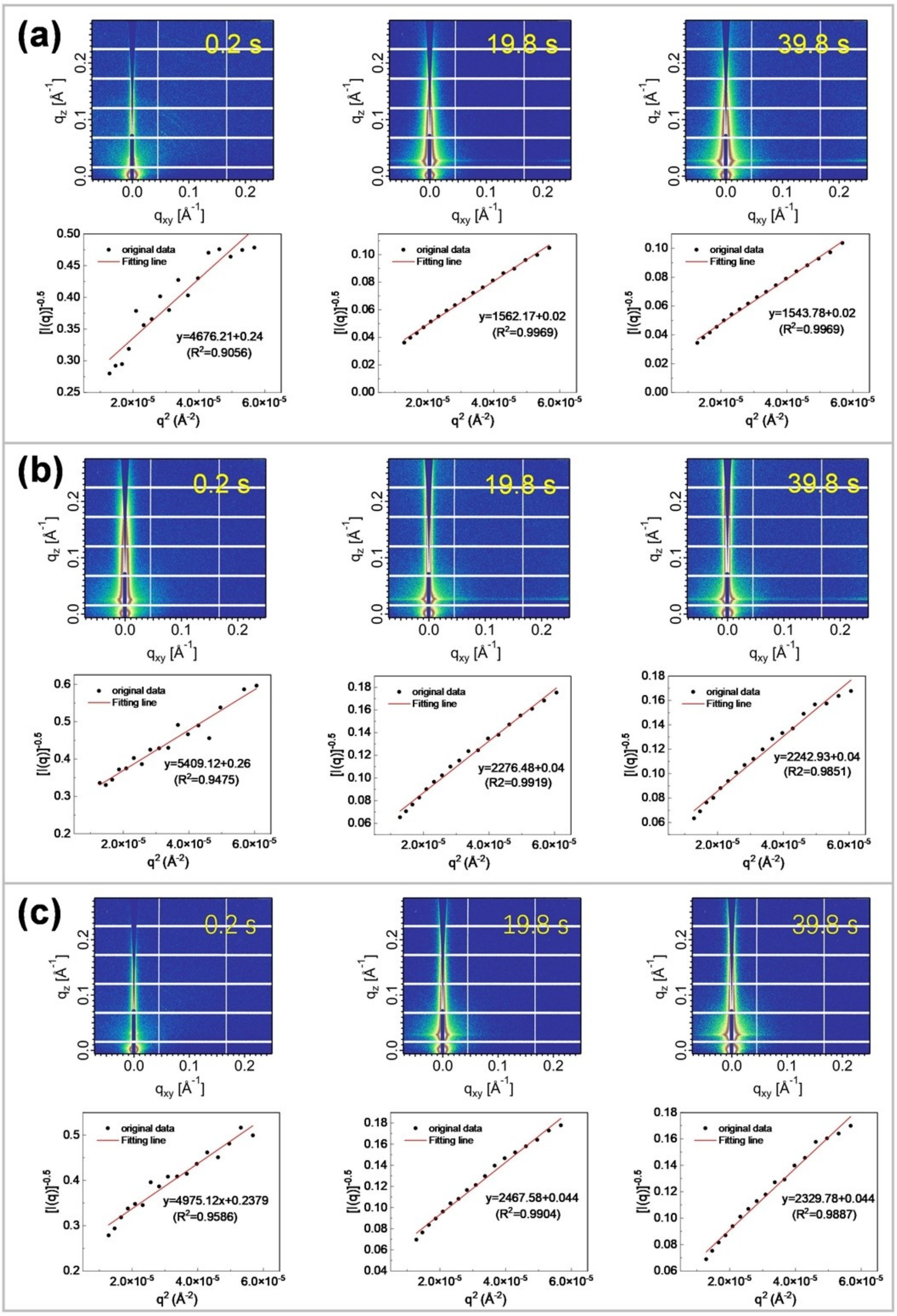

Fig. S6 Representative 2D GISAXS patterns at different time frames (initial stage: 0.2 s; intermediate stage: 19.8 s; final stage: 39.8 s) along with fits with Debye-Bueche model: (a) as-cast, (b) processed with DPE additive, and (c) processed with DIO additive.

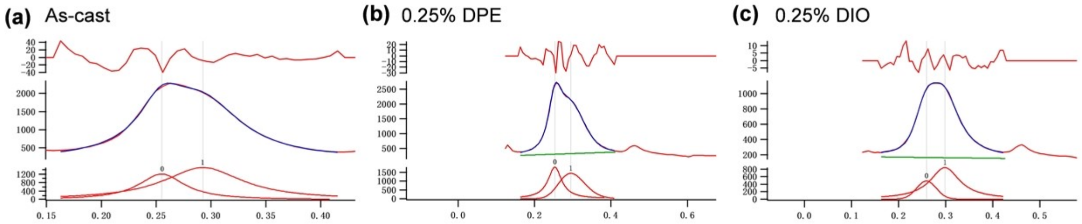

Fig. S7 Illustrations of multi-peak fitting for the lamellar reflections of the I-q curves in the IP direction: (a) as-cast, (b) with 0.25% DPE, and (c) with 0.25% DIO processed PBTA-BO:N2200 blend films.

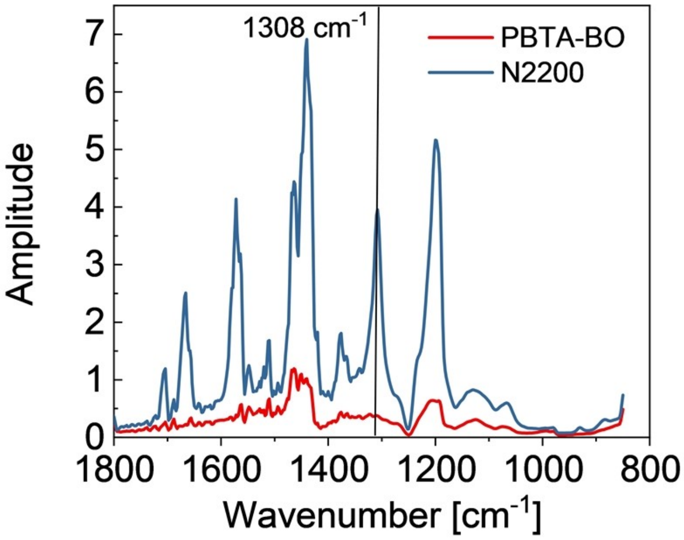

Fig. S8 IR spectra of the neat polymer thin films, where 1308 cm^{-1} was selected as the characteristic wavenumber for probing N2200.

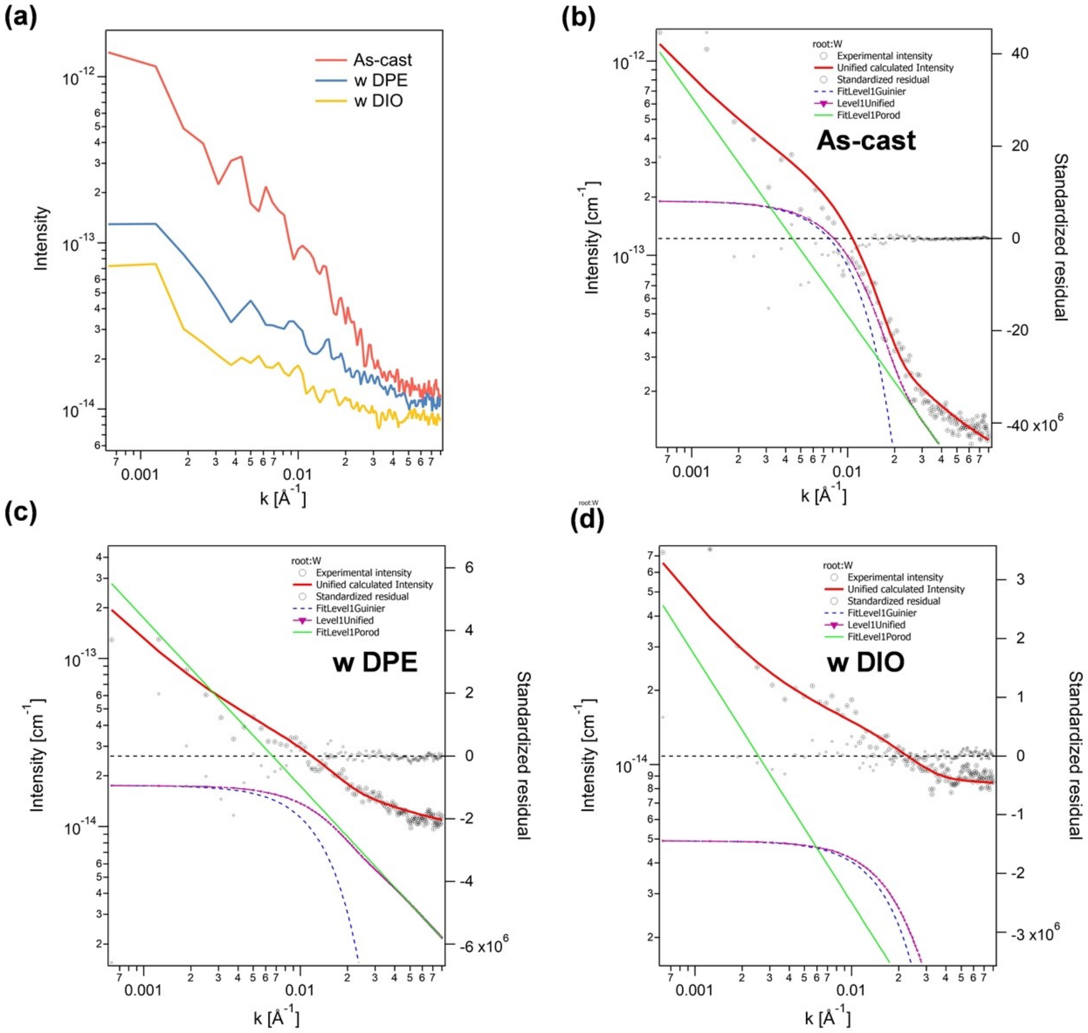

Fig. S9 (a) PSD curves derived from AFM-IR images and unified fit of *I*-*q* curves for the PSD: (b) as-cast, (c) with 0.25% DPE, and (d) with 0.25% DIO PBTA-BO:N2200 blends.

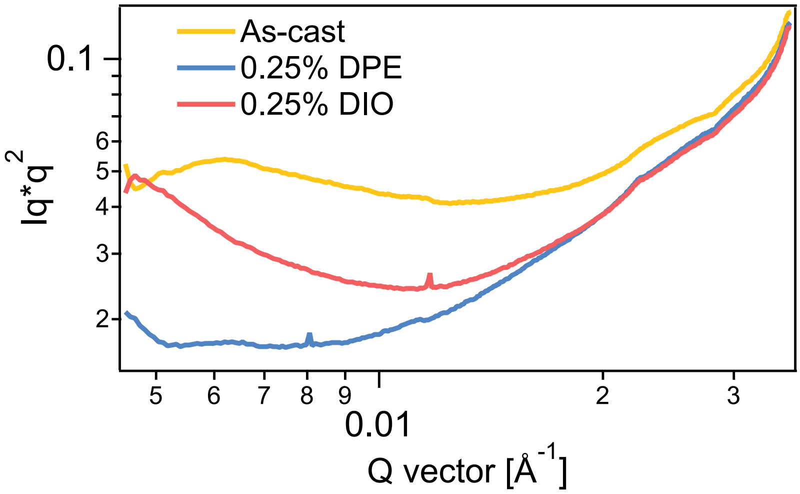

Fig. S10 RSoXS Iq^2-q curves of blend films prepared without additive and with 0.25% DPE and 0.25% DIO.

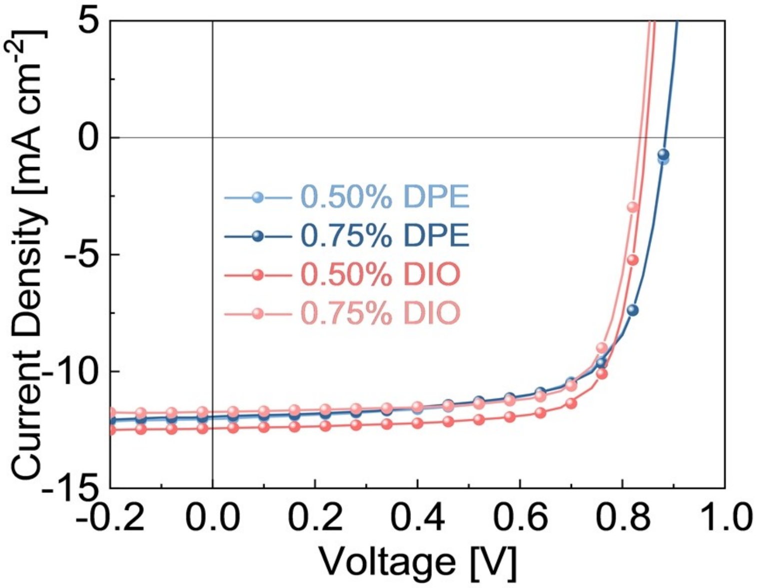

Fig. S11 *J-V* curves of PBTA-BO:N2200 all-PSCs processed with different additions of additives.

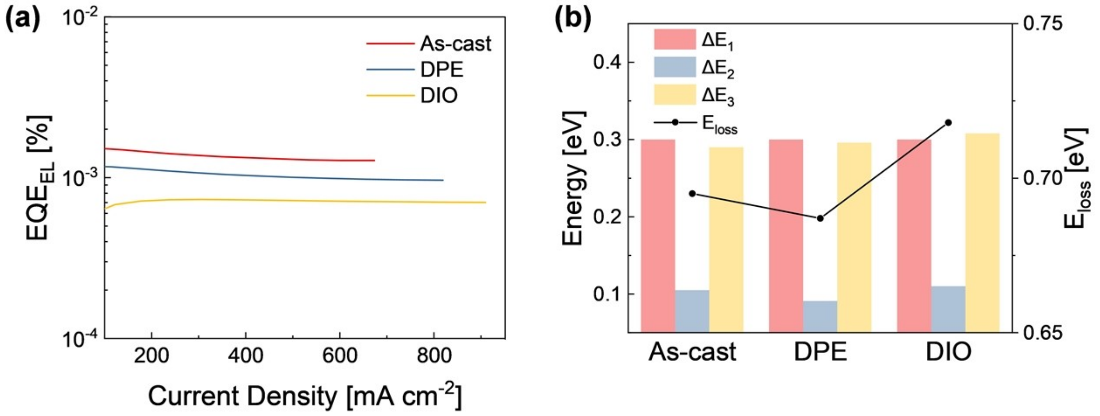

Fig. S12 (a) EL quantum efficiencies (EQE_{EL}) of the all-PSCs at various injected current densities. (b) Radiative and non-radiative energy losses in the all-PSC devices based on PBTA-BO:N2200 blends.

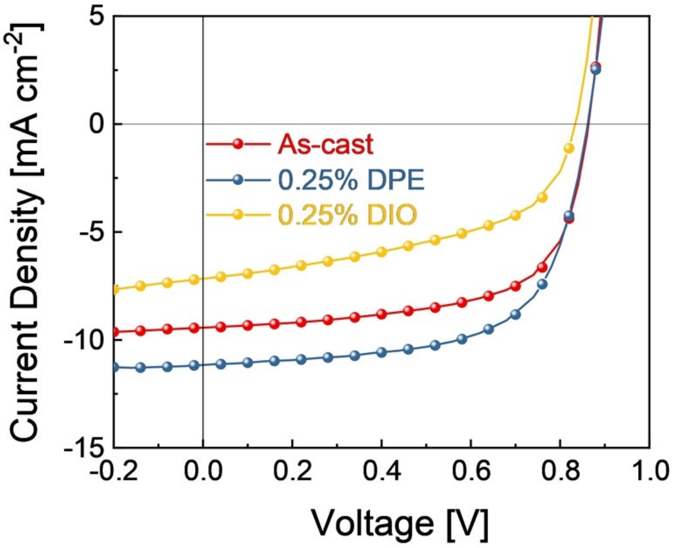

Fig. S13 *J-V* curves of all-PSCs based on PBTA-BO:N2200 blends processed with different conditions, where the additives were removed in vacuum without thermal annealing.

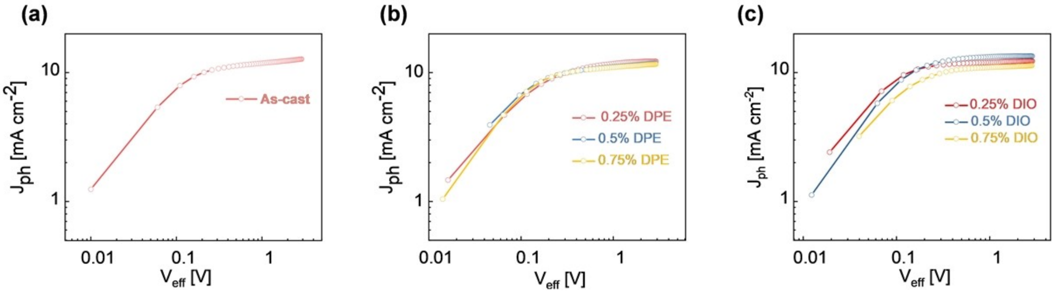

Fig. S14 J_{ph}-V_{eff} curves of PBTA-BO:N2200 all-PSCs processed with different additions of additives: (a) as-cast; (b) with DPE; (c) with DIO.

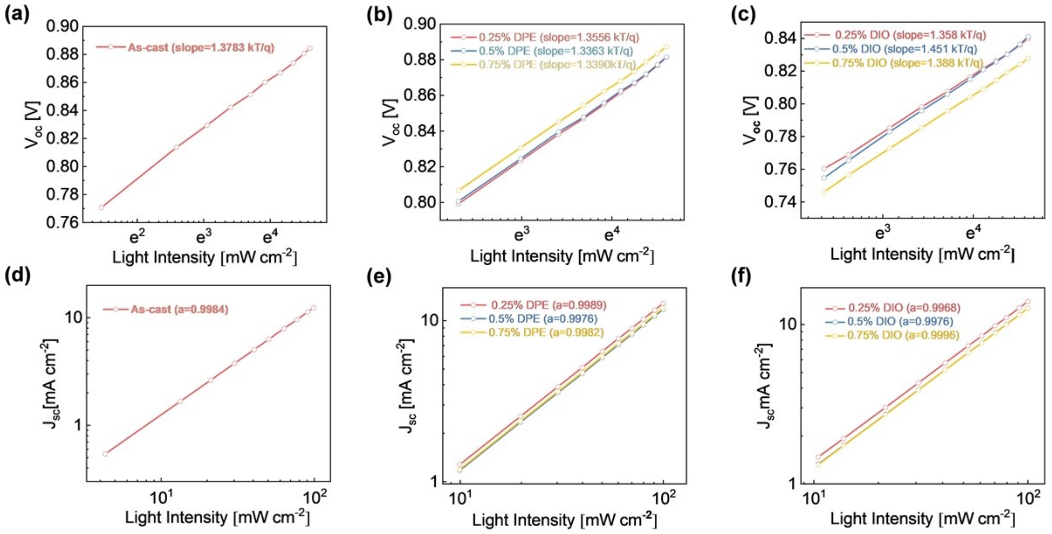

Fig. S15 Light-intensity (P_{light}) dependence of (a-c) V_{OC} and (d-f) J_{SC} of PBTA-BO:N2200 all-PSCs processed with different additions of additives.

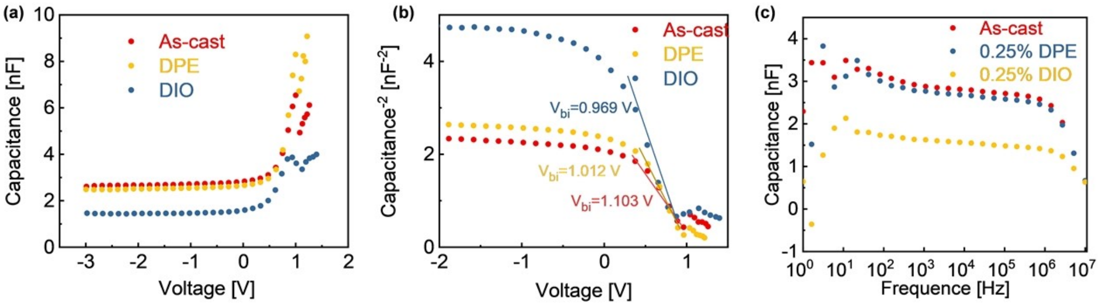

Fig. S16 (a) C-V, (b) C^{-2}-V, and (c) C-F curves of PBTA-BO:N2200 all-PSCs processed with different additions of additives.

Table S1. Summary of boiling points and polymer solubilities of MeTHF, DPE, and DIO.

Solvent or Additive	Boiling point [^{o}C]	Solubility [mg ml^{-1}]
MeTHF	79.9	PBTA-BO: 21.10
		N2200: 10.57
DPE	258	PBTA-BO: 14.77
		N2200: 6.22
DIO	338	hard to dissolve for both polymers

Table S2. Fitting result of the Unified Fit of *I-q* curves for the first frame of *in situ* GISAXS for PBTA-BO:N2200 solutions.

Solution	Fitting parameters			
	G	R_g [Å]	B	P
Additive-free	1.251	33.21	0.0196	1.11
w 0.25% DPE	1.444	34.28	0.0313	1.2
w 0.25% DIO	1.536	35.82	0.0401	1.0

Table S3. Fitting results of lamellar and π-π stacking reflection of the final frame in in situ GIWAXS.

Reflection	Thin film	d-spacing [Å]	Peak area	CCL [Å]
Lamellar	As-cast	23.315	4.322	61.502
	w DPE	23.976	8.333	68.100
	w DIO	23.387	0.761	90.302
π-π stacking	As-cast	3.766	18.560	13.926
	w DPE	3.690	18.448	15.974
	w DIO	3.759	11.312	10.695

Table S4. Fitting results of lamellar (100) and π-π stacking (010) reflection of the blend thin film in ex situ GIWAXS.

Reflection	Thin Film	Location [$Å^{-1}$]	d-spacing [Å]	Peak area	CCL [Å]
Lamellar	As-cast	0.255	24.644	95.826	123.975
		0.293	21.462	206.830	71.682
	w DPE	0.255	24.644	113.294	156.282
		0.298	21.080	225.512	73.185
	w DIO	0.258	24.284	50.245	135.21
		0.295	21.243	140.513	84.907
π-π stacking	As-cast	1.678	3.744	499.605	15.889
	w DPE	1.685	3.729	550.235	15.945
	w DIO	1.702	3.691	297.859	16.456

Table S5. Fitting results of the Unified fit for the PSD for the PBTA-BO:N2200 blends

Condition	Level 1				Level 2	
	G	R_g [Å]	B	P	B	P
As-cast	1.904e-13	152.2	2.731e-16	1	6.421e-16	1
w DPE	1.754e-14	114.7	1.736e-16	1	1.053e-16	1
w DIO	4.922e-15	77.4	2.759e-17	1	3.286e-17	1

Table S6. Photovoltaic parameters of all-PSCs based on PBTA-BO:N2200 films processed with different conditions.

Device	V_{OC} [V]	J_{SC} [mA cm^{-2}]	FF [%]	PCE [%]
As-cast	0.881 (0.882±0.005)	12.374 (12.71±0.483)	69.31 (68.41±1.50)	7.56 (7.66±0.22)
0.25% DPE	0.884 (0.881±0.003)	12.370 (12.57±0.408)	68.94 (67.06±1.66)	7.65 (7.42±0.18)
0.5% DPE	0.885 (0.882±0.004)	12.031 (11.80±0.254)	69.253 (68.7±1.43)	7.48 (7.11±0.11)
0.75% DPE	0.884 (0.884±0.002)	11.931 (11.77±0.234)	70.46 (70.33±1.30)	7.43 (7.32±0.09)
0.25% DIO	0.841 (0.842±0.003)	13.336(12.12±0.559)	75.893 (75.10±0.46)	8.53 (8.30±0.34)
0.5% DIO	0.846 (0.838±0.006)	12.430 (12.71±0.344)	76.024 (74.09±1.11)	7.99 (7.89±0.19)
0.75% DIO	0.834 (0.833±0.002)	11.725 (11.87±0.574)	76.04 (73.88±2.37)	7.44 (7.30±0.26)

Table S7. Summarized energy loss data of all-PSC devices based on PBTA-BO:N2200 blends processed with different conditions.

Device	E_g [eV]	$V_{OC,SQ}$ [V]	$V_{OC,Rad}$ [V]	V_{OC} [V]	ΔE_1 [eV]	ΔE_2 [eV]	ΔE_3 [eV]	E_{loss} [eV]	EL-EQE [%]
As-cast	1.575	1.275	1.170	0.880	0.300	0.105	0.290	0.695	1.41E-5
w DPE	1.570	1.270	1.179	0.883	0.300	0.091	0.296	0.687	1.11E-5
w DIO	1.558	1.258	1.148	0.840	0.300	0.110	0.308	0.718	7.10E-6

Table S8. Photovoltaic parameters of all-PSCs based on PBTA-BO:N2200 blends processed with different conditions, where the additives were removed in vacuum without thermal annealing.

Device	V_{OC} [V]	J_{SC} [mA cm^{-2}]	FF [%]	PCE [%]
As-cast	0.863	9.437	64.480	5.255
0.25% DPE	0.862	11.159	64.304	6.185
0.25% DIO	0.834	7.166	50.446	3.014